Original article

CO$_2$ geological sequestration in heterogeneous binary media: Effects of geological and operational conditions

Reza Ershadnia, Corey D. Wallace, Mohamad Reza Soltanian[ORCID]*

Department of Geology, University of Cincinnati, Cincinnati, OH, USA

Abstract:
Realistic representation of subsurface heterogeneity is essential to better understand and effectively predict the migration and trapping patterns of carbon dioxide (CO$_2$) during geological carbon sequestration (GCS). Many candidate aquifers for GCS have sedimentary architectures which reflect fluvial deposition, where coarser-grained facies with higher-permeability (e.g., sandstone) are juxtaposed within finer-grained facies with lower-permeability (e.g., shale). Because the subsurface is difficult to access and sample, geostatistical methods are often used to model the spatial distribution of geological facies across different scales. We use a transition-probability based approach to simulate heterogeneous systems with binary facies distributions and the resulting petrophysical properties at the field scale. The approach produces heterogeneity fields which honor observable and physical facies attributes (e.g., volumetric proportions, mean lengths, and juxtapositional tendencies). Further, we use the associated facies-dependent properties for both relative permeability and capillary pressure relations and their hysteretic behavior. Heterogeneous facies models are used to investigate the sensitivity of different trapping mechanisms (i.e., dissolution, residual trapping) as well as CO$_2$ plume dynamics to variability in (1) the spatial organization and connectivity of sedimentary facies types; (2) aquifer temperature; (3) CO$_2$ injection period; (4) perforation length; and (5) the level of impurity, represented here as methane (CH$_4$) present in injected CO$_2$ streams. Model results show that the magnitudes of residual and solubility trapping are reduced by increasing the percentage and degree of connectivity of high-permeability facies. An increase in aquifer temperature leads to a decrease in residual trapping and an increase in solubility trapping. Results also reveal that for a given volume of injected CO$_2$, shorter injection times yield higher total amounts of trapped CO$_2$. Similarly, wells perforated over a shorter thickness of the aquifer contribute to an increase in both residual and solubility trapping. We also find that increased CH$_4$ concentrations in the injected CO$_2$ streams decrease residual trapping while increasing solubility trapping. This effect is more pronounced at shallower depths, where the pressure and temperature of the aquifer are lower.

1. Introduction

Geological carbon storage (GCS) is considered a feasible option to reverse the trend of rising carbon dioxide (CO$_2$) concentrations in atmosphere (Flett et al., 2007; Oldenburg and Doughty, 2011; Li et al., 2016; Abdi-Khanghah et al., 2018; Dai et al., 2018; Amooie et al., 2019; Soltanian et al., 2019; Bemani et al., 2020a; Erfani et al., 2020; Sadatshojaie and Rahimpour, 2020; Sturmer et al., 2020). Depleted oil and gas reservoirs, un-mineable coal seams, and deep saline aquifers are among the primary candidate formations for GCS. Of these, deep saline aquifers (aquifer hereafter) are the most

preferable host as they have the highest potential for CO$_2$ storage (Bachu, 2015; Issautier et al., 2016; Hoteit et al., 2019; Menad et al., 2019). GCS is accomplished through four trapping mechanisms including structural trapping in which mobile CO$_2$ accumulates under impermeable caprocks; solubility trapping in which CO$_2$ dissolves into the in-situ brine; residual trapping in which CO$_2$ bubbles are trapped in micro-pores as an immobile phase; and mineral trapping which occurs through chemical interactions between CO$_2$, brine, and formation rock (Hassanzadeh et al., 2007; Baz et al., 2016; Soltanian and Dai, 2017; Liu et al., 2018; Singh,

2018; Dehshibi et al., 2019; Zhang et al., 2019).

The efficiency of the aforementioned trapping mechanisms is a complicated nonlinear function of various parameters, including the spatial organization and connectivity of sedimentary facies types (i.e., three-dimensional bodies of sediments) (Soltanian et al., 2015a, 2015b; Zhang et al., 2016; Liu et al., 2020), petrophysical properties (e.g., permeability and porosity distribution), and operational conditions (e.g., CO_2 injection rate and impurities in the injected CO_2 stream) (Al-Khdheeawi et al., 2018; Bahrami et al., 2020; Ershadnia et al., 2020; Bemani et al., 2020b). Although many parameters cannot be changed for a given site (i.e., geological structure, petrophysical properties), careful selection of storage sites and injection scenarios can considerably enhance the integrity of trapping mechanisms, which motivates studies of parameter sensitivity (Gershenzon et al., 2017b). Here, we analyze the sensitivity of trapping mechanisms to variability in basic parameters to provide insights into the potential for safer CO_2 storage.

Computational models have provided valuable information for evaluating the feasibility of GCS, as well as for designing and monitoring CO_2 storage operations under different scenarios (Yang et al., 2011; Hosseini et al., 2013; Hosseininooosheri et al., 2018; Sun et al., 2020). To be credible, models must accurately represent the details of geologic heterogeneity across spatial scales as well as the associated facies-dependent constitutive relations (e.g., relative permeability, capillary pressure relations, hysteretic behavior). However, previous modeling efforts have mostly simplified the influence of facies-based heterogeneity and the associated characteristic relationships on GCS and considered either homogenous or random heterogeneity models or have utilized coarse grid cells with upscaled heterogeneity properties in order to reduce computational calculations (Ide et al., 2007; Trevisan et al., 2017). These assumptions result in less accurate estimation of CO_2 plume behavior and storage capacities (Li and Benson, 2015; Baz et al., 2016).

Many candidate aquifers for GCS are located within fluvial deposition systems (Gershenzon et al., 2015a), which may exhibit sharp, discontinuous boundaries between coarse grain (CG) and fine grain (FG) cross-sets. This leads to aquifer connectivity and potentially tortuous flow pathways which control the migration and storage of CO_2 (Flett et al., 2007). Typical fluvial structure is well-captured by the transition-probability/Markov chain approach (Yang et al., 2020), which provides a feasible way to represent the facies architecture using fundamental observable attributes such as volumetric proportion, mean lengths, and juxtaposition tendency, motivating the numerical exploration of anomalous transport in fluvial systems (Carle, 1999). Using this approach, we generate two-dimensional (2D) binary models with known facies connectivity. We consider facies-dependent relative permeability and capillary pressure profiles and their hysteresis. Our main objective is to investigate the sensitivity of trapping mechanisms as well as the shape and dynamics of CO_2 plumes to selected variables, including (1) connectivity of CG facies types, (2) aquifer temperature, (3) injection period, (4) perforation length and (5) impurities in the injected CO_2 stream. For the latter,

we perform simulations at three different depths to investigate the impacts of impurity (i.e., CH_4) on CO_2 plume dynamics over a wide range of pressure and temperature conditions. In each model realization, the amounts of mobile CO_2, residually trapped CO_2, and solubility trapped CO_2 are quantified during and after injection. Although representing dominant geochemical reactions (e.g., calcite dissolution) can alter petrophysical properties (e.g., porosity and permeability) and may affect CO_2 fate and transport, we neglect mineral trapping as our simulation time is too short for accurate prediction of such kinetically-controlled processes (Doughty, 2010; Han et al., 2010).

2. Methodology

2.1 Binary facies models

The typical heterogeneity structure of fluvial systems is represented through the spatial distribution of two facies types: a CG facies type with high permeability and a FG facies type with low permeability. The spatial organization of the two facies types are generated using the transition-probability and Markov Chain approach in T-PROGS (Carle, 1999). Transition-probability is a two-point bivariate geostatistical method that considers the probability of transitioning from one facies to another. The powerful feature of this approach is its ability to producing heterogeneity models based on observable geological attributes such as proportions of each facies, mean lengths along specific directions, and juxtapositional tendencies (Amooie et al., 2017; Bianchi and Pedretti, 2017). Creating a heterogeneity model using T-PROGS is a two-step process. First, a preliminary spatial configuration of facies types is generated based on sequential indicator simulation. Then, based on a simulated quenching algorithm, a successive optimization step is performed to optimize the match between measured and simulated transition probabilities (Carle, 1999). Models created by T-PROGS have been widely used in numerical studies of subsurface flow and mass transport in hydrogeology, and in petroleum reservoirs and aquifers targeted for GCS projects (Deng et al., 2012; Sun et al., 2013; Zhou et al., 2014; Liu et al., 2020; Wallace et al., 2020; Yang et al., 2020).

Using T-PROGS, we generate 2D vertical cross-sections of an aquifer with architecture representing fluvial deposits and with different volume proportions of CG facies type ranging from 20% to 80%. Such variation is considered here to represent a wide range of conditions in natural environments (Fig. 1). The FG facies fills the rest of the domain. The aquifer length and thickness are 300 m and 40 m, respectively. The domain is discretized with a grid cell size of $\Delta x = 0.75$ m and $\Delta z = 0.1$ m (total of 160,000 grid cells) (Fig. 1). After generating facies distribution as shown in Fig. 1, permeability values of 5,000 mD and 100 mD are assigned to CG and FG facies types, respectively. We also use a positive power-law correlation (Holtz, 2002) to obtain the porosity of each facies type from the corresponding permeability values, such that the higher-permeability facies type has a higher porosity value. The resulting porosity values for CG and FG facies types are
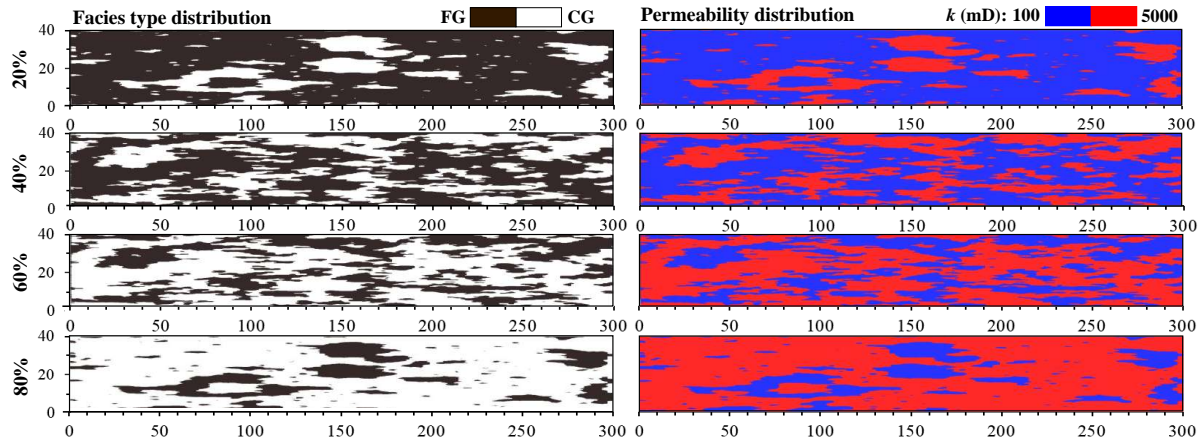
Fig. 1. Left panels show binary heterogenous media generated by T-PROGS with different proportions of CG facies type ranging from 20% to 80%. Right panels show the corresponding permeability fields. The red (respectively, blue) regions have permeability of 5,000 mD (respectively, 100 mD) and porosity of 0.34 (respectively, 0.25). The domain has dimensions of $L_x \times L_z = 300$ m $\times$ 40 m and is discretized by a fine 400×400 element mesh.
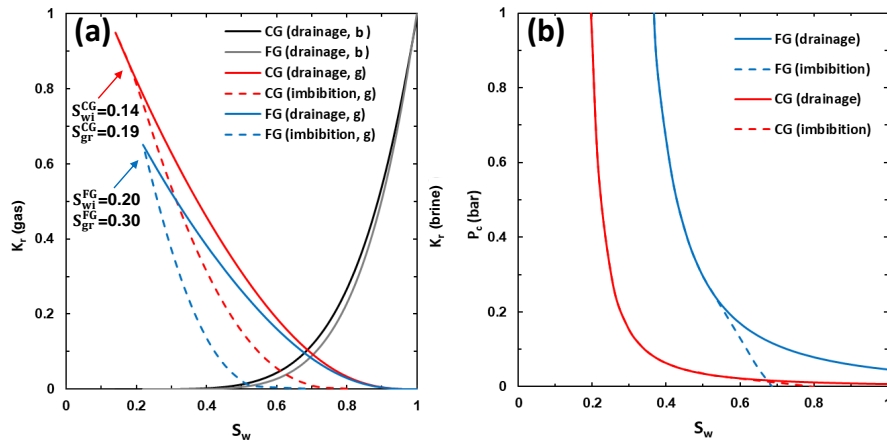

Fig. 2. (a) Relative permeability and (b) capillary pressure curves for FG and CG cross-sets for both drainage and imbibition processes. The *g* and *b* stand for gas and brine phase, respectively.

0.34 vs. 0.25.

Facies connectivity is controlled by the volume proportion (Gershenzon et al., 2015b, 2015c; Soltanian et al., 2020). As per percolation theory, randomly placed grid cells of a given facies type have at least one connected tortuous pathway through a cluster spanning opposing boundaries if their volume proportion is at or above the 2D percolation threshold of 59.3% (Stauffer and Aharony, 1992). Here, the aquifer models will range from those with a dominant number of high-permeability CG cells connected in one spanning cluster to those with no spanning cluster. Therefore, comparison between the heterogeneity models is useful for quantifying how the connectivity of CG facies type affects GCS, specifically the spatial distribution of CO_2 plume.

2.2 Modeling approach

We use CMG-GEM to perform equation of state (EOS)-based two-phase flow simulations (CMG, 2018). CMG-GEM is a multidimensional, finite-difference, and compositional simulator capable of modeling carbon sequestration in a fully coupled framework (e.g., advective and dispersive flow), and has been successfully used in previous modeling studies of different GCS projects worldwide (Kim et al., 2017; Hosseini-noosheri et al., 2018; Soltanian et al., 2019; Sun et al., 2020). The generated indicator data from T-PROGS and the resulting permeability and porosity distributions are incorporated into the computational grid of CMG-GEM.

Different constitutive relations (e.g., capillary pressure and relative permeability curves) are used for FG and CG facies to properly represent different multiphase flow dynamics (Fig. 2). The values of average irreducible water saturation (S_{wi}) and the maximum residual gas saturation (S_{gr}^{max}) are calculated using the following equations (Holtz, 2002):

$$S_{wi} = 5.159(\log(k)\phi)^{-1.559} \tag{1}$$

$$S_{gr}^{max} = -0.969\phi + 0.5473 \tag{2}$$

where k[-] and ϕ[-] are the permeability and porosity of each facies type, respectively. The relationship between saturation and drainage portion of relative permeability curves is defined

by the Brooks-Corey function as (Brooks and Corey, 1966):

$$k_{r,w}^{Dr} = \left(\frac{S - S_{wi}}{1 - S_{wi}} \right)^{N_w} \qquad (3)$$

$$k_{r,g}^{Dr} = k_{r,g}(S_{wi}) \left(1 - \frac{S - S_{wi} - S_{gcr}}{1 - S_{gr} - S_{wi} - S_{gcr}} \right)^2 \\ \left[1 - \left(1 - \frac{S - S_{wi} - S_{gcr}}{1 - S_{gr} - S_{wi} - S_{gcr}} \right)^{N_g} \right] \qquad (4)$$

where S[-] is water saturation, S_{gr}[-] is the residual gas saturation, and S_{gcr}[-] is the critical gas saturation. S_{gcr} is 0.04 for both FG and CG cross strata. The N_w[-] and N_g[-] reflect pore-size distributions. For drainage processes, N_w and N_g are set to 5 and 4, respectively (Gershenzon et al., 2017b).

Since brine is the wetting phase, its relative permeability curves are considered the same for both drainage and imbibition processes (Kumar et al., 2005; Juanes et al., 2006; Taggart, 2010). In contrast, CO_2 is the non-wetting phase and its relative permeability depends on whether CO_2 is displacing or being displaced by brine. The gas relative permeability hysteresis is modeled in this work using Killough's approach (Killough, 1976).

$$k_{r,g} = \begin{cases} k_{r,g}^{Dr}(S_g) & \text{drainage} \\ k_{r,g}^{Dr}(S_g(shifted)) & \text{imbibition} \end{cases} \qquad (5)$$

where $S_g(shifted)$ is calculated as:

$$S_g(shifted) = S_{gr} + \frac{S_{gh} - S_{gr}}{S_{gh} - S_{grh}}(S_g - S_{grh}) \qquad (6)$$

and

$$\frac{1}{S_{grh} - S_{gr}} - \frac{1}{S_{gh} - S_{gr}} = \frac{1}{S_{gr}^{max} - S_{gr}} - \frac{1}{S_g^{max} - S_{gr}} \qquad (7)$$

where S_{gr}[-] is residual gas saturation. S_{gh} is equal to S_g when the shift to imbibition occurs (i.e., gas saturation at brine reversal), and S_{grh} is the value of S_{gr} corresponding to S_{gh} within Land's equation (Land, 1968). S_g^{max}[-] is equal to $1 - S_{wr}$ (Kumar et al., 2005). Values of S_{gr}^{max} for CG and FG facies types are found through Eq. (2).

The capillary pressure curves for the drainage process are also constructed based on the Brooks-Corey function (Brooks and Corey, 1966):

$$P_{cd} = P_e \left(\frac{S - S_{wi}}{1 - S_{wi}} \right)^{\frac{-1}{\lambda}} \qquad (8)$$

where P_{cd}[bar] is the capillary pressure for drainage process, P_e[bar] is capillary entry pressure (or the displacement pressure), and S[-] is water saturation. The values of S_{wi}[-] for each facies type are calculated by Eq. (1). The λ[-] is the pore size distribution index for the Brooks-Corey model. The values of P_e and λ for the FG facies type are specified as $P_e = 0.046$ bar and $\lambda = 0.55$, following the values used in Gershenzon et al. (2017b). The entry pressure for the CG facies is calculated by scaling the values for FG rocks using the Leverett J-function

Table 1. Hydraulic and geometric parameters of aquifer.

Property	Value
Hydraulic properties	
CG permeability (K_{CG})	5,000 mD
CG porosity (ϕ_{CG})	0.37
FG permeability (K_{FG})	100 mD
FG porosity (ϕ_{FG})	0.25
Aquifer pressure	32.06 MPa
Pore size distribution index (λ)	0.55
P_{entry} of CG	7.3×10^{-3} bar
P_{entry} of FG	4.6×10^{-2} bar
S_{gi}^{max} of CG	0.19
S_{gi}^{max} of FG	0.30
S_{wi} of CG	0.14
S_{wi} of FG	0.20
$K_{rg}(S_{wi})$ of CG	0.95
$K_{rg}(S_{wi})$ of FG	0.65
Geometric properties	
Model length (L_x)	300 m
Model thickness (L_z)	40 m
Model discretization ($\Delta L_x \times \Delta L_z$)	0.75 m × 0.1 m
Depth to surface	2,260 m

(Saadatpoor et al., 2010):

$$P_e^{CG} = P_e^{FG} \left(\frac{k_{FG} \phi_{CG}}{k_{CG} \phi_{FG}} \right)^{0.5} \qquad (9)$$

For imbibition, a curve analogous to the drainage curve (Eq. (8)) is used, with the difference that the imbibition curve crosses the saturation axis at a value of $S = 1 - S_{gr}$ (Fig. 2(b)). The imbibition capillary pressure curves are estimated with the residual gas saturation selected to be consistent with the values of 0.3 and 0.19 used for the residual gas saturation in the relative permeability functions. Table 1 provides all the variables of the relative permeability and capillary pressure curves for each facies type.

2.3 Modelled scenarios

A baseline scenario is considered to serve as a reference for assessing the impact of (1) facies connectivity, (2) aquifer temperature, (3) CO_2 injection period, (4) perforation length, and (5) impurity of the injected CO_2 stream, on spatial evolution and CO_2 trapping capacities. In the baseline scenario, pure CO_2 is injected into a binary heterogeneous aquifer with 60% volume proportion of CG facies types. The rest of the aquifer is occupied by FG facies type. The CO_2 injection rate is set to 22.6 kg/min for 10 days, which corresponds to a total injected volume of $\sim$ 325 tons. The top of the aquifer is located 2,260
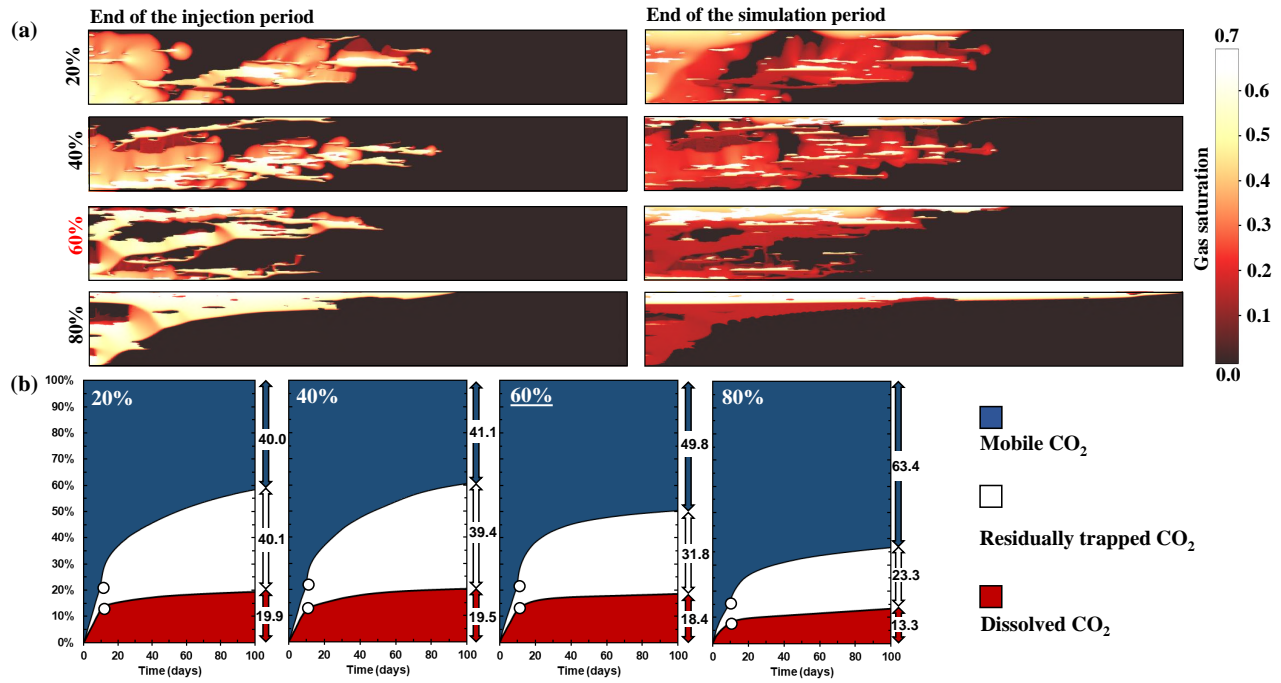
Fig. 3. (a) Saturation profiles for systems with different proportions of CG materials ranging from 20% to 80%, and (b) mass distribution of injected CO_2 as a function of simulation time. White circles show values of dissolved and residually trapped CO_2 at the end of the injection period.

m below the ground surface. CO_2 is injected through the bottom 4 m of the domain at the left side of the aquifer. The CO_2 plume dynamics are monitored during injection and for 90 days post-injection (100-day simulation time). The injection rates and the total volume of CO_2 injected are specified so that CO_2 breakthrough does not occur in displacements with high gravity forces, where CO_2-rich bank easily reaches the right aquifer boundary. The initial pressure and temperature in the middle of aquifer are 32.06 MPa and 130 °C, respectively. These conditions ensure that the CO_2 is injected in its super-critical state. The grid scale in permeability anisotropy ratio (k_v/k_h) is set at 0.1. For all simulations presented herein, the top and bottom sides of the storage domain are bounded by impermeable layers, and other sides are open to flow following the approach used by Juanes et al. (2006) and Soltanian et al. (2019). Table 2 provides the physical properties used to define the basic scenario and range of parameters used in the other scenarios.

3. Results and discussion

3.1 Connectivity of CG materials

Here, we examine how juxtaposition of CG and FG facies types, as well as preferential flow pathways created by CG connectivity, affect the spatial pattern of CO_2 plume and the efficiency of trapping mechanisms. We compare simulations with different proportions of CG facies ranging from 20% to 80% in increasing increments of 20%. Heterogeneity models with 20% and 40% CG volume proportions do not have full connectivity, while aquifer models with 60% and 80% volume proportions of CG facies are fully connected. Results show that

Table 2. Parameters for the baseline scenario and sensitivity analysis.

Scenario range	Baseline scenario	Parameter
Volume proportion of CG	60%	20%−80%
Aquifer temperature	130 °C	90−170 °C
Perforation length	4 m	1−16 m
Injection period	10 Days	2−50 Days
Injection composition	100% CO_2	80%−100%
	0% CH_4	0 %−20%

the aquifer with the highest volume proportion has the lowest residual and solubility trapping capacities (Fig. 3), which may lead to higher risks of CO_2 leakage.

Fig. 3(a) shows the gas saturation profiles at the end of injection (left panels) and post-injection (right panels) periods. Fig. 3(b) shows the mass distribution of injected CO_2 as a function of time. During the injection period, the ratio of viscous to gravity forces along with the organization of facies types defines the CO_2 plume dynamics (Gershenzon et al., 2015a). The injected CO_2 preferentially enters the higher permeability CG clusters. In case with 80% volume proportion where CG facies are perfectly connected, the CO_2 plume reaches the top of the aquifer in 2 days and then spreads laterally underneath the cap rock. In case with 20% volume proportion, however, the plume is laterally stretched within the aquifer and does not reach the top due to the increasingly tortuous flow pathways created by FG facies types. Indeed, FG facies types act as barrier to slow the upward migration of CO_2 and thereby enhance the CO_2-brine contact area, resulting

in larger solubility trapping (Fig. 3).

After injection ceases, viscous forces become negligible and CO_2 transport is governed by gravity and capillary forces. Rising CO_2 can easily penetrate from FG to CG facies type because at a given CO_2 saturation, P_c in FG facies is always larger than the capillary entry pressure (P_e) in overlain CG facies (see Fig. 2). Thus, the fate of migrated CO_2 in CG facies is strongly controlled by the spatial organization and degree of connectivity of CG facies types.

In non-percolating cases (volume proportions of 20% and 40%), the CO_2 plume cannot migrate from underlying CG (i.e., smaller P_e) to overlying FG facies (i.e., larger P_e) unless the summation of P_c in the CG facies and the buoyant force per area of facies is more than the P_e in FG facies type (Gershenzon et al., 2016). The process by which a CO_2 plume locally accumulates below FG layers (with larger-than-average P_e) as a volume of connected and potentially mobile phase is referred to as capillary pinning (Saadatpoor et al., 2010; Gershenzon et al., 2017a). The imbibition of brine into pore spaces that are filled with capillary-pinned CO_2 leads to accelerated entrapment of the gaseous CO_2, resulting in high residual trapping in non-percolating cases (compare 20% and 40% cases in Fig. 3(b)). The results also show negligible differences between these two non-percolating cases in the integral characteristics, i.e., residual and solubility trapping, which means in non-percolating cases the proportion of CG facies types does not significantly affect the efficiency of trapping mechanisms (Fig. 3(b)).

In percolating (60% and 80% CG) cases, much of the gaseous CO_2 migrates upwards into and through next sets of CG facies above and accumulates under the cap rock. Results show that in the 60% case, the distribution of CO_2 is relatively dominated by capillary heterogeneity, which causes plume stretching and increases the CO_2-brine contact area. In contrast, for the 80% case, the rising CO_2 plume does not experience much channeling and tends to bypass the low-permeability FG facies on its way up. Thus, from 60% to 80% volume proportion (i.e., above the percolation threshold), the distribution of CO_2 changes from relatively ramified and channeled to smooth and uniform, and both residual and solubility trapping decrease (compare 60% and 80% cases in Fig. 3(b)).

Based on these results, we conclude that increasing the proportion of CG facies types leads to a decrease in both residual and solubility trapping, an unfavorable result from a sequestration point of view. In non-percolating cases, there is a negligible decrease in trapping mechanisms, while percolating cases show a sharp decline.

3.2 Aquifer temperature

To assess the impact of aquifer temperature on CO_2 storage and its spatial evolution, we simulate our baseline scenario at different aquifer temperatures ranging from 90 to 170 °C in increasing increments of 20 °C. Previous experimental studies have shown that the solubility of CO_2 in brine varies with temperature. At relatively low pressures (<10 MPa),

CO_2 solubility decreases gradually with temperature, while at higher pressures (>10 MPa) it increases with temperature (Duan and Sun, 2003). Our simulation results show that the rise in aquifer temperature from 90 to 170 °C results in an increase in the amount of solubility trapping (from $\sim$ 14% to $\sim$ 22%) and a decrease in residual trapping (from $\sim$ 35% to $\sim$ 27%) (Fig. 4).

Increasing temperature affects the solubility trapping in two ways. First, the mole fraction of CO_2 in the aqueous phase increases from 0.018 to 0.026 when the temperature increases from 90 to 170 °C at 32.06 MPa. These values are consistent with those reported in the literature for pure brine (Duan and Sun, 2003). Second, the density of CO_2 decreases and, since the same total mass of CO_2 is injected in every case, the volume occupied by the injected CO_2 becomes larger, resulting in more CO_2 being dissolved into brine (compare plume sizes in Fig. 4(a)). Considering these two effects, increasing the aquifer's temperature leads to more solubility trapping. This result is consistent with conclusions drawn by Kumar et al. (2005) and Al-Khdheeawi et al. (2018).

Unlike solubility trapping, there is an inverse correlation between residual trapping and aquifer temperature. Differences in the amount of residually trapped CO_2 result from the differences in the plume distributions at the end of the injection period. At high temperatures, much of the gas leaves the lower part of the aquifer uninvaded and flows upwards as soon as it is injected. This forms a layer of mobile plume in the upper half of the aquifer due to the increased density contrast between CO_2 and native brine (Fig. 4(a)). Therefore, on average, the volume of gas pinned below low-permeability layers prior to brine reversal is reduced, which limits the residually trapped CO_2 during the post-injection phase. The opposite is true in low temperature cases. Therefore, increasing aquifer temperature, corresponding to increasing gravity forces, has a negative effect on residual trapping. Our findings are in agreement with results of work by Ide et al. (2007), who showed increasing gravity forces reduces the residual trapping capacity.

In summary, increasing the aquifer temperature increases solubility trapping and reduces residual trapping. However, because these two trapping mechanisms are correlated, their competing impacts tend to cancel out, leaving the CO_2 storage capacity relatively insensitive to aquifer temperature.

3.3 Injection period

To assess the effect of injection period on CO_2 storage and its spatial evolution, we perform five different simulations with varying the injection periods of 2, 5, 10, 20, and 50 days, while keeping all other parameters constant. Fig. 5 illustrates how trapping capacities are affected by these injection periods. Note that total injected mass is the same for all cases and only the injection period varies, which results in different injection rates. Results indicate that a shorter injection period (higher injection rate) leads to less mobile CO_2 reaching the top of the storage formation. This benefits both solubility and residual trapping.

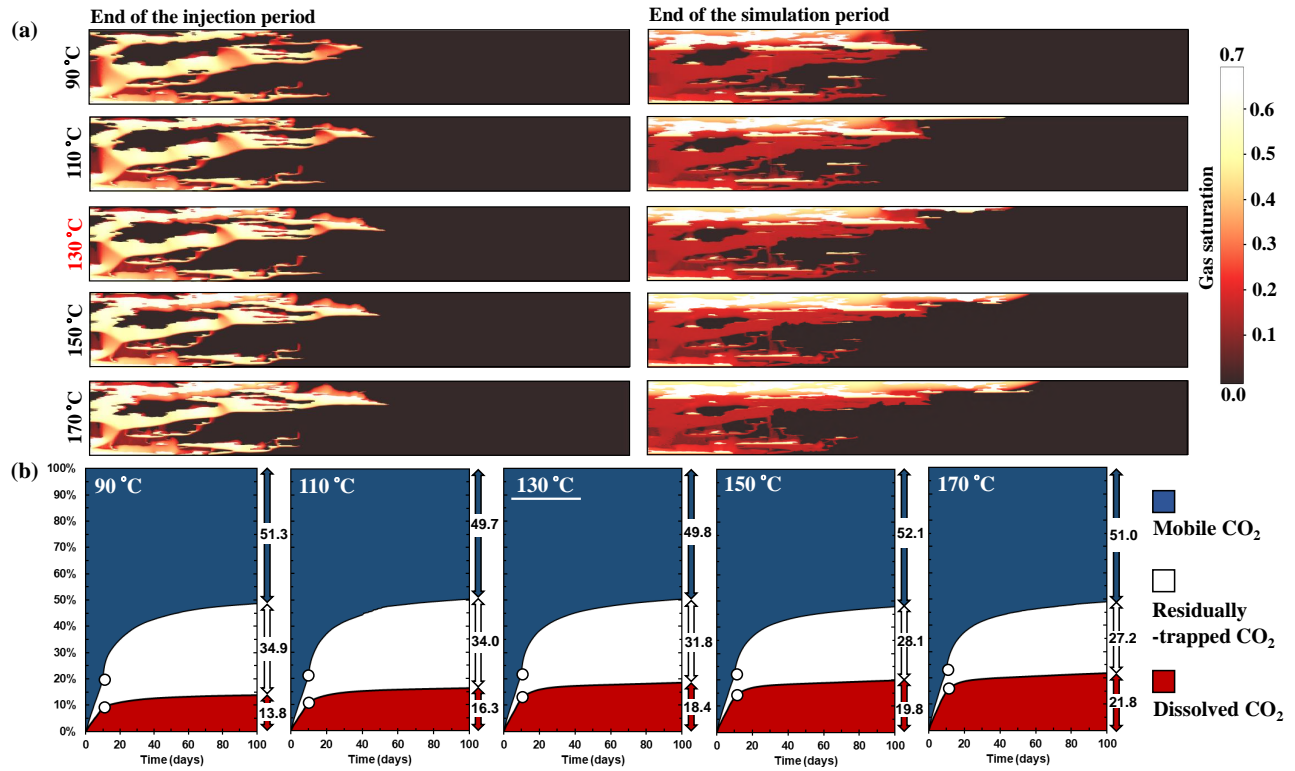With a short injection period, the viscous forces are en-

Fig. 4. (a) Saturation profiles at various aquifer's temperatures ranging from 90 to 170 °C, and (b) mass distribution of injected CO_2 as a function of simulation time. White circles show values of dissolved and residually trapped CO_2 at the end of the injection period.
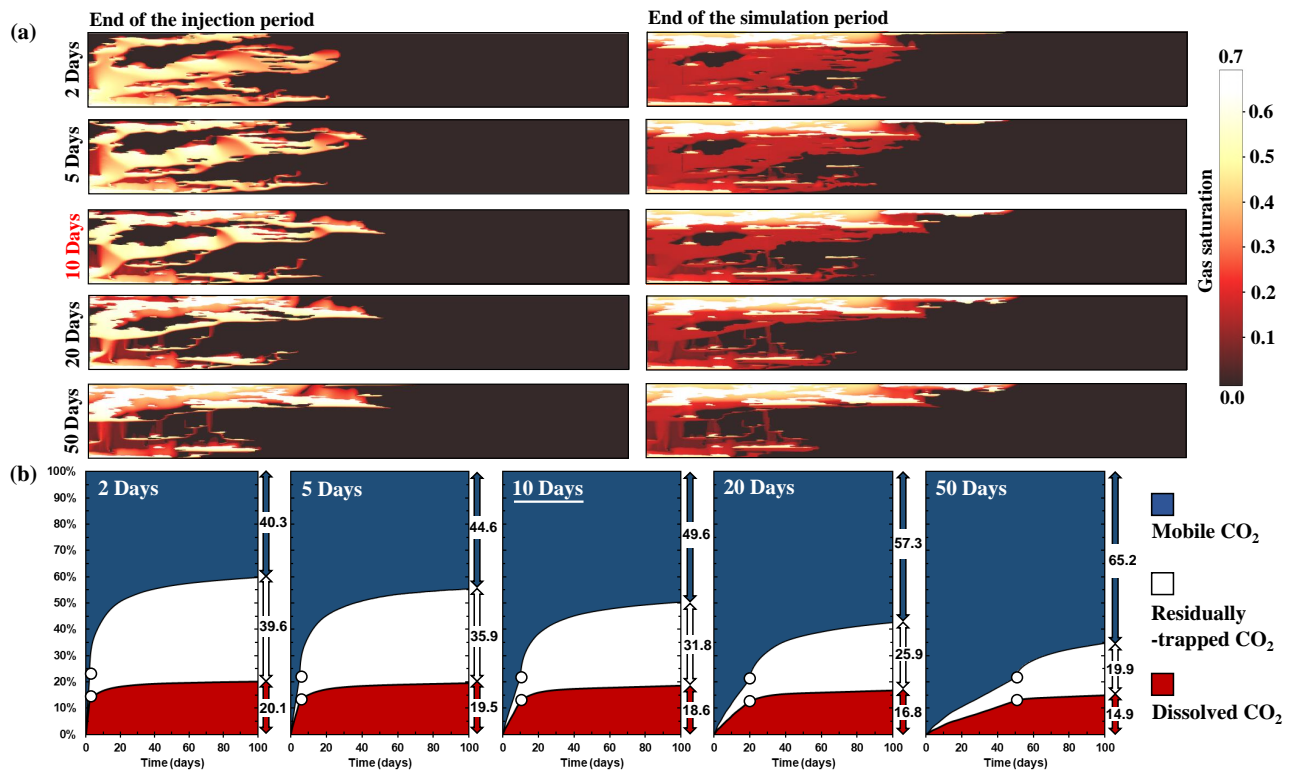

Fig. 5. (a) Saturation profiles for various injection periods ranging from 2 to 50 days, and (b) mass distribution of injected CO_2 as a function of simulation time. White circles show values of dissolved and residually trapped CO_2 at the end of the injection period.
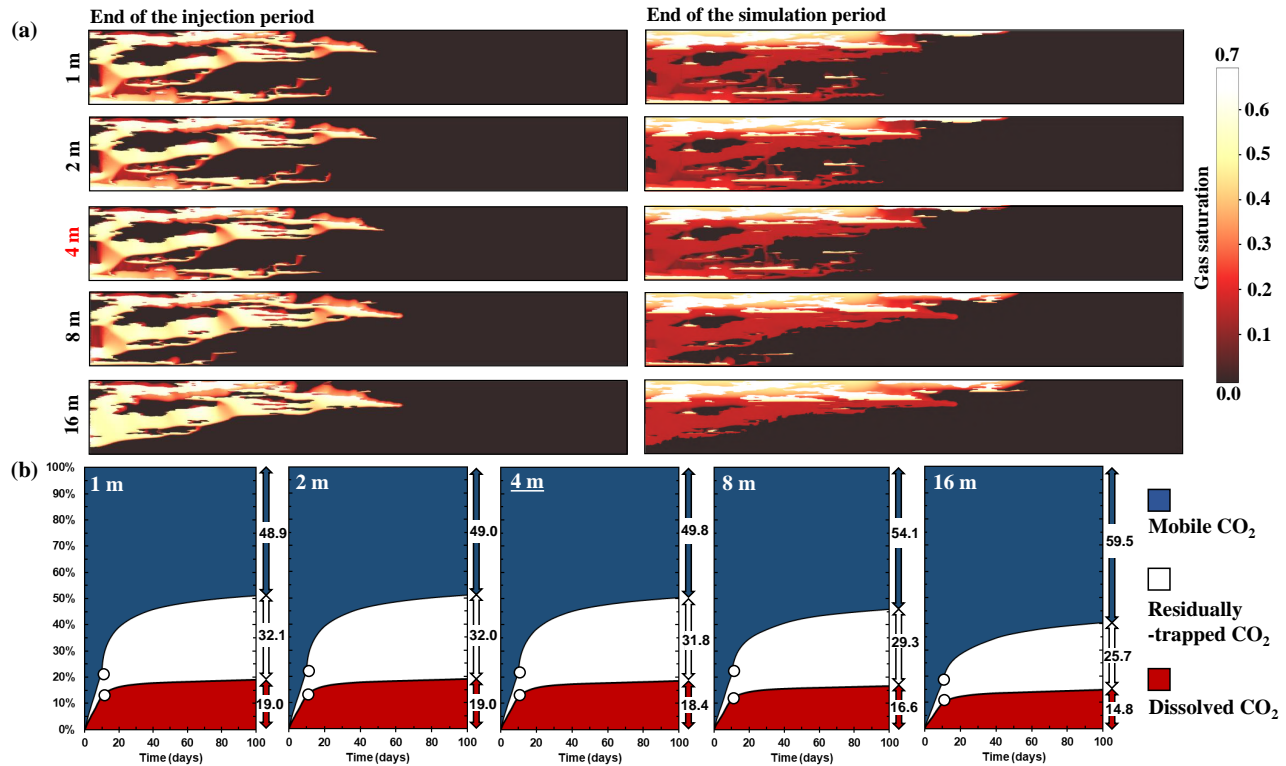
Fig. 6. (a) Saturation profiles for various perforation lengths ranging from 1 to 16 m, and (b) mass distribution of injected CO_2 as a function of simulation time. White circles show values of dissolved and residually trapped CO_2 at the end of the injection period.

hanced at least in the vicinity of wellbores. The increased viscous forces carry the gas laterally in the lower portions of aquifer. The expansion of the plume in horizontal direction increases the CO_2-brine contact area, which, in turn, leads to larger solubility trapping. In contrast, during longer injection periods, the gravity forces are comparable to or even larger than viscous forces during injection phase. Under this condition, much of the injected gas quickly migrates upwards into and through channels of correlated larger-than-average permeability, where capillary entry pressure is locally smaller than average. The CO_2 that occupies the top layers remains mobile so long as injection continues, causing a reduction in storage capacity.

Once injection ends, the rest of the mobile CO_2 within the aquifer starts moving upwards from its present position due to the dominance of gravity forces. This mobile CO_2 invades the previously uncontacted brine. Since the lateral extension of the CO_2 plume is shorter at the end of injection phase in cases with longer injection periods, a smaller volume of uncontacted brine is invaded by rising CO_2 and less solubility trapping is obtained. Further, on average, the amount of mobile gas that is pinned in aquifer before brine reversal is decreased. Thus, the brine imbibes back into pore spaces filled with smaller amounts of CO_2, reducing the post-injection residual trapping. Recall that a downward trend in the amount of residually trapped CO_2 is seen as injection period increases. The opposite behavior is noticed during short injection periods.

It should be noted that maximizing the trapping capacities by reducing the injection period increases the maximum well

bottom-hole pressure (BHP), which is a major disadvantage. Results show that decreasing the injection period from 50 days to 2 days increases the BHP from 38.4 to 41.4 MPa. If injection pressure exceeds the rock fracturing pressure, the integrity of caprock may be compromised. Thus, it is essential to keep the BHP below 90% of fracture pressure at the depth of perforation (Baz et al., 2016).

In summary, our results show that increasing the injection period, corresponding to decreasing injection rate, increases CO_2 mobility and decreases both residual and solubility trapping. However, choosing the optimum injection period involves a trade-off between injectivity, BHP, and the efficiency of trapping mechanisms.

3.4 Perforation interval

To examine how CO_2 dynamics and storage capacities respond to the perforation interval, we modify the baseline scenario using four different lengths of perforation: 1 m, 2 m, 8 m, and 16 m. Perforations are started at bottom of the injection well. For instance, the 16 m interval corresponds to perforating the bottom 40% of aquifer thickness, and 4 m (the baseline scenario) corresponds to perforation across the bottom 10% of aquifer thickness. We observe that there are, respectively, 6% and 4% reductions in residual and solubility trapping as perforated length increases from 1 to 16 m (Fig. 6).

When the process of CO_2 injection is started, the gaseous CO_2 occupies the wellbore. Since injected CO_2 is less dense

than brine residing in the aquifer (580 kg/m^3 vs. 968 kg/m^3), there is a difference in the hydrostatic pressure gradient (HPG) between the wellbore and the aquifer. HPG is the rate of change in fluid pressure with depth, and its values for pure CO_2 and aquifer materials are 5.7 kPa/m and 9.5 kPa/m, respectively. The difference in HPG means that the upper perforations experience a higher pressure difference between the wellbore and aquifer compared to the lower perforations (see Kumar adn Bryant (2008)). For instance, in the case of a 16 m perforation interval, the difference between wellbore pressure and aquifer pressure is $\sim$ 7.08 MPa at the bottom-most perforation, while the difference increases to 7.15 MPa at the top-most perforation. Thus, the upper perforations allow a larger volume of injected CO_2 into the aquifer due to the higher pressure difference. The extent of this effect decreases with decreasing the length of perforated interval.

The preferential migration of CO_2 through upper perforations can clearly be seen in the 16 m perforated interval scenario, where the bottom $\sim$ 3 m of perforation interval does not contribute to CO_2 injection (Fig. 6(a), left panel). To confirm that this observation is irrespective of spatial connectivity of CG facies types, we simulate the same scenario in non-percolating heterogeneity models (volume proportions of 20% and 40%) and indeed observe no difference in results (not shown). The higher flow of CO_2 into upper perforations has two negative effects on the capacity of trapping mechanisms. First, the CO_2 plume does not come into contact with brine around bottom perforations, decreasing the amount of CO_2 dissolved into brine. Second, the CO_2 plume travels a shorter path to reach the top seal, which reduces the residual trail left behind and thereby decreases residually trapped CO_2 during the post-injection period. In contrast, in case of a 1 m interval, the pressure difference between the wellbore and aquifer is almost constant across the perforated interval, and thus all perforations contribute to CO_2 injection throughout the injection phase, resulting in enhanced lateral spreading area of CO_2 plume around lower portions of the aquifer and, in turn, increased solubility trapping (Fig. 6(a)). In addition, the distribution of CO_2 near the bottom perforations benefits residual trapping during the post-injection period because CO_2 migrates a longer distance before reaching the uppermost zone of the aquifer (compare case 1 m and 16 m in Figs. 6(a) and 6(b)). However, injecting CO_2 through a smaller perforated interval also increases the BHP, which can endanger the integrity of trapping mechanisms. A decrease in total amount of CO_2 immobilized with increase in perforation interval has also been reported by prior studies (Kumar and Bryant, 2008; Han et al., 2010; Baz et al., 2016).

We conclude that for a desired injection volume, an optimum perforation length should be selected so that (1) the whole length of the perforated interval contributes to injection throughout the injection phase, and (2) the injectivity does not compromise the containment of the target formation. This optimum perforation length should be placed at the bottom-most interval of the aquifer to maximize the distance between the top perforation and the top of the aquifer, leading to increased residual and solubility trapping.

3.5 Impurity level in injected CO_2 stream

CO_2 captured from the emitters includes various impurities such as CH_4. Although co-injection of impurities with CO_2 may have undesirable effects on CO_2 storage capacity, it drastically reduces the cost of carbon storage (Wang et al., 2012; Mahmoodpour et al., 2020). In this section, we analyze how changing the impurity level of CH_4 in injected CO_2 influences plume migration dynamics as well as the efficiency of trapping mechanisms. The mole fraction of CH_4 in the injection stream ranges from 0% (our baseline scenario) to 20% in 5% increments. A first observation, controlling the shape and dynamics of the plume associated with CH_4 impurity is that viscosity and density of CH_4-CO_2 mixtures are lower than those of pure CO_2 at a given temperature and pressure. However, the viscosity and density contrasts between the CO_2-CH_4 mixtures and pure CO_2 crucially depends on the pressure and temperature of the aquifer (Nicot et al., 2013). In order to investigate the effect of CH_4 impurity on CO_2 geological storage over a wide range of pressure and temperature, we perform simulations for three depths: "shallow" (depth of 565 m, temperature of $\sim$ 32 °C and pressure $\sim$ 8 MPa), "median" (depth of 1,130 m, temperature of 65 °C and pressure $\sim$ 16 MPa) and "deep" (depth of 2,260 m, temperature of 130 °C and pressure $\sim$ 32 MPa) (Table 3). The storage capacity of the aquifer in each case is calculated with respect to the total amount of injected CO_2. Results show that at a certain depth, with increasing CH_4 fraction in the injected stream, both the horizontal migration distance and upward movement of the plume are enhanced, resulting in more solubility trapping and less residual trapping compared with the pure-CO_2 case. Our results are shown in Figs. 7-9 and are discussed below.

Considering that the viscosity of CH_4 is lower than that of CO_2, the presence of CH_4 would result in higher mobility and thus faster horizontal migration of the injected stream (Figs. 7-9). As a result, the higher the CH_4 content in the injected stream, the larger the contact area between brine and the plume, giving rise to enhanced solubility trapping (Figs. 7-9). In addition to the viscosity contrast, CH_4 is less soluble in brine than CO_2, leading to an accumulation of CH_4 at the edge of the gas plume. The partitioning between CH_4 and CO_2 may be used as a safety alarm for monitoring the procedures of possible leakage, since high-purity CH_4 would be detected earlier than CO_2 if leakage occurs and provide time for remediation of leakage (Hosseini et al., 2012). The density of CH_4 is also less than that of CO_2, and the inclusion of CH_4 impurity benefits the upward migration of injected gas. As a consequence, the contribution of CH_4 impurity on residual trapping is negative, as much of the injected gas reaches the top of the aquifer and accumulates below the caprock before brine imbibition occurs in the post-injection period (Figs. 7-9).

The viscosity and density contrasts between mixtures and pure CO_2 decreases with depth (Table 3). For instance, at shallow depths when CH_4 concentration is 20%, the density decreases by about 47% and viscosity decreases by over 45% compared with pure CO_2, while these values are, respectively, about 20% and 12% at "deep" cases (Table 3). Streams with
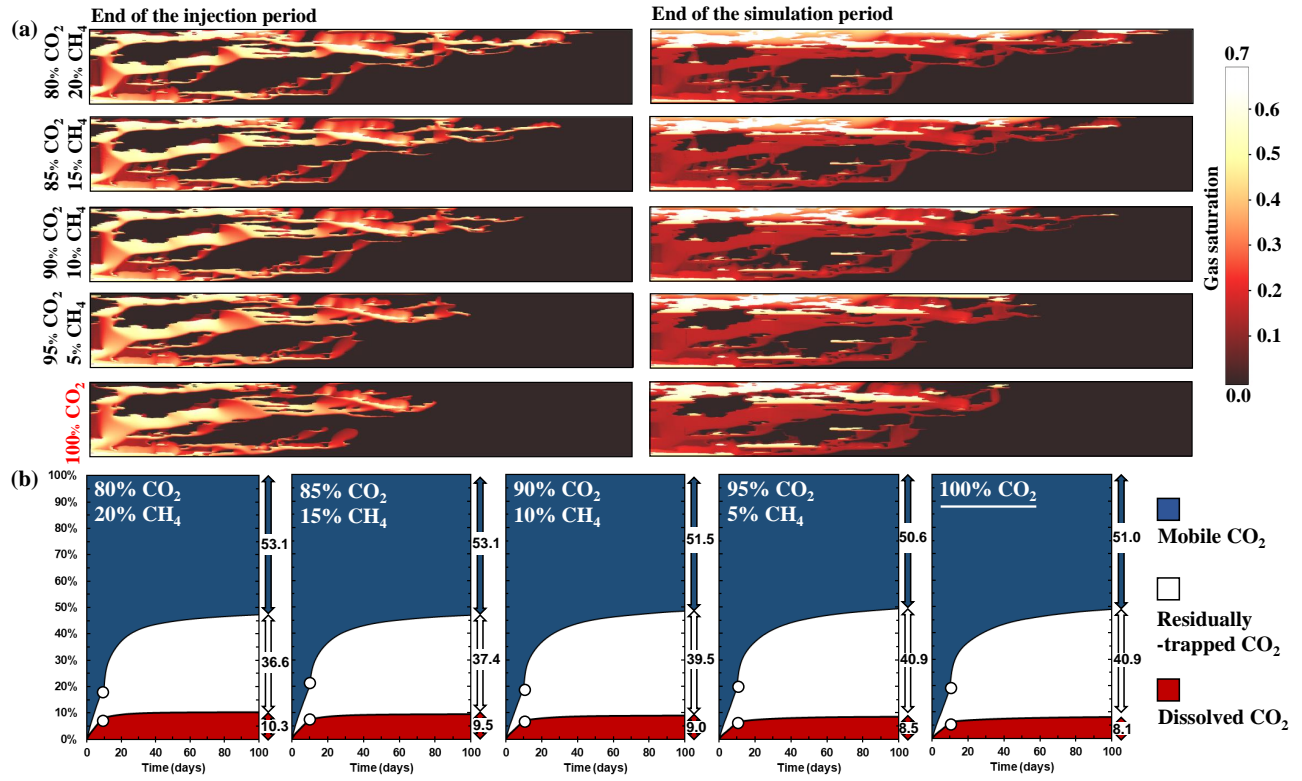
Fig. 7. (a) Saturation profiles for various proportions of CH_4 in injected CO_2 streams at shallow depth (Table 3), and (b) mass distribution of injected CO_2 as a function of simulation time. White circles show values of dissolved and residually trapped CO_2 at the end of the injection period.

Fig. 8. (a) Saturation profiles for various proportions of CH_4 in injected CO_2 streams at median depth (Table 3), and (b) mass distribution of injected CO_2 as a function of simulation time. White circles show values of dissolved and residually trapped CO_2 at the end of the injection period.
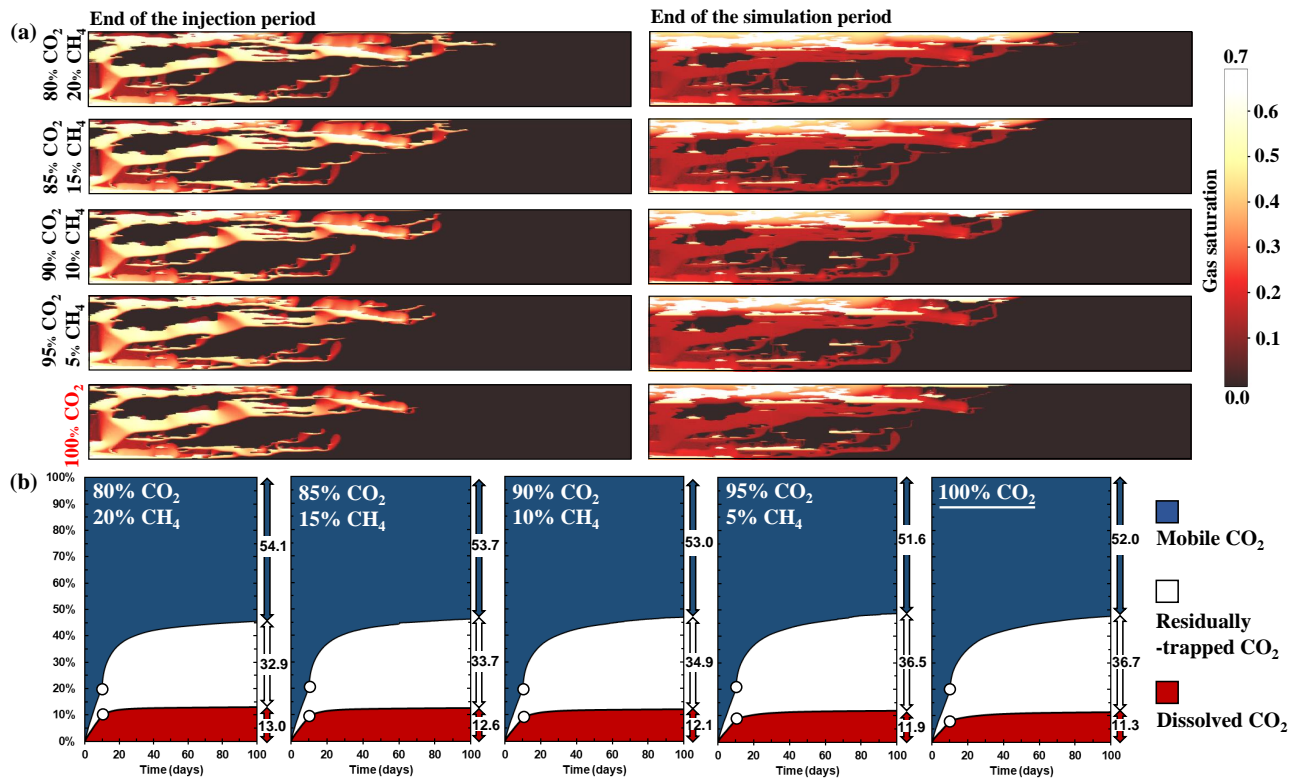
Fig. 9. (a) Saturation profiles for various proportions of CH_4 in injected CO_2 streams at deep depth (Table 3), and (b) mass distribution of injected CO_2 as a function of simulation time. White circles show values of dissolved and residually trapped CO_2 at the end of the injection period.
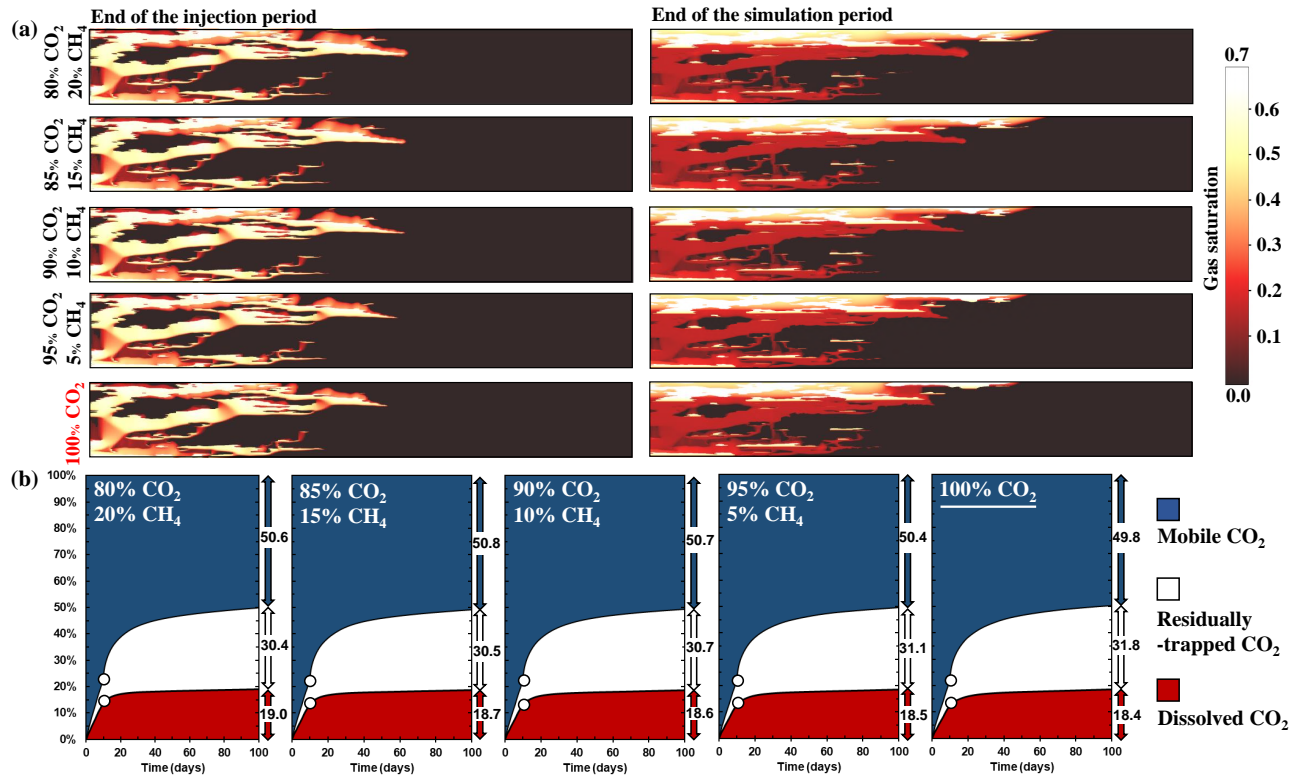
Table 3. Characteristics of shallow, median, and deep models.

Scenarios	Depth (m)	P (MPa)	T (°C)	Injection composition (mole%)	ρ (kg/m^3)	μ (Pa·s)	BHP_{max} (MPa)
Shallow depth	565	8.01	32.5	100% CO_2	690.4	5.5×10^{-5}	14.4
Shallow depth	565	8.01	32.5	95% CO_2 with 5% CH_4	599.1	4.7×10^{-5}	14.8
Shallow depth	565	8.01	32.5	90% CO_2 with 10% CH_4	500.5	3.9×10^{-5}	15.0
Shallow depth	565	8.01	32.5	85% CO_2 with 15% CH_4	426.1	3.3×10^{-5}	15.2
Shallow depth	565	8.01	32.5	80% CO_2 with 20% CH_4	366.8	3.0×10^{-5}	16.0
Median depth	1130	16.03	65	100% CO_2	605.5	4.8×10^{-5}	22.4
Median depth	1130	16.03	65	95% CO_2 with 5% CH_4	551.1	4.4×10^{-5}	22.9
Median depth	1130	16.03	65	90% CO_2 with 10% CH_4	501.4	4.0×10^{-5}	23.0
Median depth	1130	16.03	65	85% CO_2 with 15% CH_4	456.5	3.8×10^{-5}	23.4
Median depth	1130	16.03	65	80% CO_2 with 20% CH_4	418.1	3.5×10^{-5}	23.6
Deep depth	2260	32.06	130	100% CO_2	580.0	4.8×10^{-5}	39.3
Deep depth	2260	32.06	130	95% CO_2 with 5% CH_4	547.5	4.7×10^{-5}	39.5
Deep depth	2260	32.06	130	90% CO_2 with 10% CH_4	516.9	4.5×10^{-5}	39.5
Deep depth	2260	32.06	130	85% CO_2 with 15% CH_4	488.6	4.3×10^{-5}	39.7
Deep depth	2260	32.06	130	80% CO_2 with 20% CH_4	461.3	4.2×10^{-5}	39.9

lower CH_4 contents would exhibit smaller changes in the density and viscosity. For solubility (respectively, residual) trapping, the greatest positive (respectively, negative) effect of impurity occurs at shallow depth and for 20% CH_4 (Fig. 7). Under this condition, the leading edge of the injected stream reaches about 280 m at the end of injection period, while it only reaches about 190 m in the pure CO_2 case (Fig. 7(a)). This difference becomes even larger in the post-injection period. Similarly, the maximum gas saturation accumulated below the caprock by the end of injection period is about 0.67 in case with 20% CH_4 impurity and decreases by 0.54 in the pure CO_2 case, resulting in reduced residual trapping (Fig. 7). On the contrary, the effects of CH_4 impurity on the plume distribution and trapping capacities can hardly be observed in deep aquifers (Fig. 9). The dependence of trapping capacities as well as saturation profiles on the depth of aquifer is clear through comparison of Figs. 7-9.

However, since CH_4 significantly reduces the density of the injected stream, higher flow pressure is required to achieve the same mass flow rate as for the pure CO_2 case (Table 3). The BHP at shallow depth increases from 14.4 to 16 MPa when CH_4 concentration increases from 0% to 20%, which indicates the necessity of imposing a restriction on the CH_4 content in the injected stream (Table 3). This is particularly critical during the injection period, when the containment of the target formation may be compromised by aquifer over-pressurization, which would lead to new fractures or cause slip along pre-existing faults in the caprock.

In summary, increasing the CH_4 content in the injected CO_2 stream (1) benefits the CO_2 solubility trapping, (2) decreases the CO_2 residual trapping, and (3) increases the BHP. These impacts are more marked at shallow depths, where the contrast in density and viscosity with pure CO_2 are largest.

4. Conclusions

We perform a series of high-resolution and 2D numerical simulations to analyze the sensitivity of CO_2 trapping capacity as well as the shape and dynamics of CO_2 plumes to variability in the spatial organization and connectivity of sedimentary facies types, aquifer temperature, CO_2 injection period, perforation length, and level of CH_4 impurities in injected CO_2 streams. For each case, the values of trapped (residual and dissolved) and mobile CO_2 are quantified. The major conclusions of this study are as follows:

1) The amount of residually and solubility trapped CO_2 are reduced by increasing the degree of connectivity of high-permeability CG facies types.
2) An increase in aquifer temperature leads to an increase in solubility trapping and a decrease in residual trapping, whereas their effects on storage capacity tend to cancel out, leaving the mobile CO_2 unchanged.
3) Increasing the injection period, corresponding to a decreased injection rate, results in a reduction in both solubility and residual trapping.
4) The shorter perforation length shows higher solubility and residual trapping.
5) The presence of CH_4 impurities in injected CO_2 streams

increases solubility trapping and decreases residual trapping. These impacts are more marked at shallower depths, where aquifer's temperature and pressure are lower.

Acknowledgement

Conflict of interest

The authors declare no competing interest.

References

Abdi-Khanghah, M., Bemani, A., Naserzadeh, Z., et al. Prediction of solubility of n-alkanes in supercritical CO_2 using rbf-ann and mlp-ann. J. CO_2 Util. 2018, 25: 108-119.

Abubakar, A., Habashy, T.M. .Three-dimensional single-well imaging of the multi-array triaxial induction logging data, in SEG Technical Program Expanded Abstracts 2006, Society of Exploration Geophysicists, Tulsa, pp. 411-415, 2006.

Al-Khdheeawi, E.A., Vialle, S., Barifcani, A., et al. Effect of wettability heterogeneity and reservoir temperature on CO_2 storage efficiency in deep saline aquifers. Int. J. Greenhouse Gas Control 2018, 68: 216-229.

Amooie, M.A., Hemmati-Sarapardeh, A., Karan, K., et al. Data-driven modeling of interfacial tension in impure CO_2-brine systems with implications for geological carbon storage. Int. J. Greenhouse Gas Control 2019, 90: 102811.

Bachu, S. Review of CO_2 storage efficiency in deep saline aquifers. Int. J. Greenhouse Gas Control 2015, 40: 188-202.

Bahrami, B., Sadatshojaie, A., Wood, D.A. Assessing wellbore stability with a modified lade failure criterion. J. Energy Resour. Technol. 2020, 142(8): 083004.

Baz, H., Noureldin, M., Allinson, W., et al. A field-scale investigation of residual and dissolution trapping of CO_2 in a saline formation in western australia. Int. J. Greenhouse Gas Control 2016, 46: 86-99.

Bemani, A., Baghban, A., Mohammadi, A.H., et al. Estimation of adsorption capacity of CO_2, CH_4, and their binary mixtures in quidam shale using lssvm: Application in CO_2 enhanced shale gas recovery and CO_2 storage. J. Nat. Gas Sci. Eng. 2020a, 76: 103204.

Bemani, A., Baghban, A., Mosavi, A. Estimating CO_2-brine diffusivity using hybrid models of anfis and evolutionary algorithms. Eng. Appl. Comput. Fluid Mech. 2020b, 14(1): 818-834.

Bianchi, M., Pedretti, D. Geological entropy and solute transport in heterogeneous porous media. Water Resour. Res. 2017, 53(6): 4691-4708.

Brooks, R.H., Corey, A.T. Properties of porous media affecting fluid flow. J. Irrig. Drain. Div. 1966, 92(2): 61-90.

Carle, S.F. T-progs: Transition probability geostatistical software. Livermore, University of California, Davis, 1999.

CMG, GEM Advanced Compositional and Unconventional Reservoir Simulator Version 2018. CMG Ltd., C.M. Group, Editor. 2018.

Dai, Z., Zhang, Y., Bielicki, J., et al. Heterogeneity-assisted carbon dioxide storage in marine sediments. Appl. Energy 2018, 225: 876-883.

Dehshibi, R.R., Sadatshojaie, A., Mohebbi, A., et al. A new insight into pore body filling mechanism during waterflooding in a glass micro-model. Chem. Eng. Res. Des. 2019, 151: 100-107.

Deng, H., Stauffer, P.H., Dai, Z., et al. Simulation of industrial-scale CO_2 storage: Multi-scale heterogeneity and its impacts on storage capacity, injectivity and leakage. Int. J. Greenhouse Gas Control 2012, 10: 397-418.

Doughty, C. Investigation of CO_2 plume behavior for a large-scale pilot test of geologic carbon storage in a saline formation. Transp. Porous Media 2010, 82(1): 49-76.

Duan, Z., Sun, R. An improved model calculating CO_2 solubility in pure water and aqueous nacl solutions from 273 to 533 k and from 0 to 2000 bar. Chem. Geol. 2003, 193(3-4): 257-271.

Erfani, H., Babaei, M., Niasar, V. Signature of geochemistry on density-driven CO_2 mixing in sandstone aquifers. Water Resour. Res. 2020, 56(3): e2019WR026060.

Ershadnia, R., Amooie, M.A., Shams, R., et al. Non-newtonian fluid flow dynamics in rotating annular media: Physics-based and data-driven modeling. J. Pet. Sci. Eng. 2020, 185: 106641.

Flett, M., Gurton, R., Weir, G. Heterogeneous saline formations for carbon dioxide disposal: Impact of varying heterogeneity on containment and trapping. J. Pet. Sci. Eng. 2007, 57(1-2): 106-118.

Gershenzon, N.I., Ritzi Jr, R.W., Dominic, D.F., et al. Influence of small-scale fluvial architecture on CO_2 trapping processes in deep brine reservoirs. Water Resour. Res. 2015a, 51(10): 8240-8256.

Gershenzon, N.I., Ritzi Jr, R.W., Dominic, D.F., et al. Comparison of CO_2 trapping in highly heterogeneous reservoirs with brooks-corey and van genuchten type capillary pressure curves. Adv. Water Resour. 2016, 96: 225-236.

Gershenzon, N.I., Ritzi Jr, R.W., Dominic, D.F., et al. Capillary trapping of CO_2 in heterogeneous reservoirs during the injection period. Int. J. Greenhouse Gas Control 2017a, 59: 13-23.

Gershenzon, N.I., Ritzi Jr, R.W., Dominic, D.F., et al. CO_2 trapping in reservoirs with fluvial architecture: Sensitivity to heterogeneity in permeability and constitutive relationship parameters for different rock types. J. Pet. Sci. Eng. 2017b, 155: 89-99.

Gershenzon, N.I., Soltanian, M., Ritzi, R.W., et al. Understanding the impact of open-framework conglomerates on water–oil displacements: The victor interval of the ivishak reservoir, prudhoe bay field, alaska. Pet. Geosci. 2015b, 21(1): 43-54.

Han, W.S., Lee, S.Y., Lu, C., et al. Effects of permeability on CO_2 trapping mechanisms and buoyancy-driven CO_2 migration in saline formations. Water Resour. Res. 2010, 46(7): W07510.

Hassanzadeh, H., Pooladi-Darvish, M., Keith, D.W. Scaling behavior of convective mixing, with application to geological storage of CO_2. AICHE J. 2007, 53(5): 1121-1131.

Holtz, M. Residual gas saturation to aquifer influx: A calculation method for 3-d computer reservoir model construction. Paper SPE 75502 Presented at SPE Gas Technology Symposium, Calgary, Alberta, Canada, 30 April-2 May, 2002.

Hosseini, S.A., Lashgari, H., Choi, J.W., et al. Static and dynamic reservoir modeling for geological CO_2 sequestration at cranfield, mississippi, USA. Int. J. Greenhouse Gas Control 2013, 18: 449-462.

Hosseini, S.A., Mathias, S.A., Javadpour, F. Analytical model for CO_2 injection into brine aquifers-containing residual CH_4. Transp. Porous Media 2012, 94(3): 795-815.

Hosseininoosheri, P., Hosseini, S., Nuñez-López, V., et al. Impact of field development strategies on CO_2 trapping mechanisms in a CO_2-EOR field: A case study in the permian basin (sacroc unit). Int. J. Greenhouse Gas Control 2018, 72: 92-104.

Hoteit, H., Fahs, M., Soltanian, M.R. Assessment of CO_2 injectivity during sequestration in depleted gas reservoirs. Geosciences 2019, 9(5): 199.

Ide, S.T., Jessen, K., Orr Jr, F.M. Storage of CO_2 in saline aquifers: Effects of gravity, viscous, and capillary forces on amount and timing of trapping. Int. J. Greenhouse Gas Control 2007, 1(4): 481-491.

Issautier, B., Viseur, S., Audigane, P., et al. A new approach for evaluating the impact of fluvial type heterogeneity in CO_2 storage reservoir modeling. C. R. Geosci. 2016, 348(7): 531-539.

Juanes, R., Spiteri, E., Orr Jr, F., et al. Impact of relative permeability hysteresis on geological CO_2 storage. Water Resour. Res. 2006, 42(12): W12418.

Killough, J. Reservoir simulation with history-dependent saturation functions. Soc. Petrol. Eng. J. 1976, 16(1): 37-48.

Kim, Y., Jang, H., Kim, J., et al. Prediction of storage efficiency on CO_2 sequestration in deep saline aquifers using artificial neural network. Appl. Energy 2017, 185: 916-928.

Kumar, A., Noh, M.H., Ozah, R.C., et al. Reservoir simulation of CO_2 storage in aquifers. SPE J. 2005, 10(3): 336-348.

Kumar, N., Bryant, S. Optimizing injection intervals in vertical and horizontal wells for CO_2 sequestration. Paper SPE 116661 Presented at SPE Annual Technical Conference and Exhibition, Denver, Colorado, USA, 21-24 September, 2008.

Land, C.S. Calculation of imbibition relative permeability for two-and three-phase flow from rock properties. Soc. Petrol. Eng. J. 1968, 8(2): 149-156.

Li, B., Benson, S.M. Influence of small-scale heterogeneity on upward CO_2 plume migration in storage aquifers. Adv. Water Resour. 2015, 83: 389-404.

Li, C., Zhang, K., Wang, Y., et al. Experimental and numerical analysis of reservoir performance for geological CO_2 storage in the ordos basin in china. Int. J. Greenhouse Gas Control 2016, 45: 216-232.

Liu, B., Fu, X., Li, Z. Impacts of CO_2-brine-rock interaction on sealing efficiency of sand caprock: A case study of shihezi formation in ordos basin. Adv. Geo-Energy Res. 2018, 2(4): 380-392.

Liu, Y., Wallace, C.D., Zhou, Y., et al. Influence of streambed heterogeneity on hyporheic flow and sorptive solute transport. Water 2020, 12(6): 1547.

Mahmoodpour, S., Amooie, M.A., Rostami, B., et al. Effect of gas impurity on the convective dissolution of CO_2 in porous media. Energy 2020, 199: 117397.

Menad, N.A., Hemmati-Sarapardeh, A., Varamesh, A., et al. Predicting solubility of CO_2 in brine by advanced machine learning systems: Application to carbon capture and sequestration. J. CO_2 Util. 2019, 33: 83-95.

Nicot, J.P., Solano, S., Lu, J., et al. Potential subsurface impacts of CO_2 stream impurities on geologic carbon storage. Energy Procedia 2013, 37: 4552-4559.

Oldenburg, C., Doughty, C. Injection, flow, and mixing of CO_2 in porous media with residual gas. Transp. Porous Media 2011, 90(1): 201-218.

Saadatpoor, E., Bryant, S.L., Sepehrnoori, K. New trapping mechanism in carbon sequestration. Transp. Porous Media 2010, 82(1): 3-17.

Sadatshojaie, A., Rahimpour, M.R. CO_2 emission and air pollution (volatile organic compounds, etc.)–related problems causing climate change, in Current Trends and Future Developments on (Bio-) Membranes, edited by A. Figoli, Y. Li and A. Basile, Elsevier, Amsterdam, pp. 1-30, 2020.

Singh, H. Impact of four different CO_2 injection schemes on extent of reservoir pressure and saturation. Adv. Geo-Energy Res. 2018, 2(3): 305-318.

Soltanian, M.R., Behzadi, F., de Barros, F.P. Dilution enhancement in hierarchical and multiscale heterogeneous sediments. J. Hydrol. 2020, 587: 125025.

Soltanian, M.R., Dai, Z. Geologic CO_2 sequestration: Progress and challenges. Geomech. Geophys. Geo-Energy Geo-Resour. 2017, 3: 221-223.

Soltanian, M.R., Hajirezaie, S., Hosseini, S.A., et al. Multicomponent reactive transport of carbon dioxide in fluvial heterogeneous aquifers. J. Nat. Gas Sci. Eng. 2019, 65: 212-223.

Soltanian, M.R., Ritzi, R.W., Huang, C.C., et al. Relating reactive solute transport to hierarchical and multiscale sedimentary architecture in a Lagrangian-based transport model: 1. Time-dependent effective retardation factor. Water Resour. Res. 2015a, 51(3): 1586-1600.

Soltanian, M.R., Ritzi, R.W., Huang, C.C., et al. Relating reactive solute transport to hierarchical and multiscale sedimentary architecture in a Lagrangian-based transport model: 2. Particle displacement variance. Water Resour. Res. 2015b, 51(3): 1601-1618.

Stauffer, D., Aharony, A. Introduction To Percolation Theory: Revised Second Edition. London, UK, Taylor & Francis, 1992.

Sturmer, D.M., Tempel, R.N., Soltanian, M.R. Geological carbon sequestration: Modeling mafic rock carbonation using point-source flue gases. Int. J. Greenhouse Gas Control 2020, 99: 103106.

Sun, Q., Ampomah, W., Kutsienyo, E.J., et al. Assessment of CO_2 trapping mechanisms in partially depleted oil-bearing sands. Fuel 2020, 278: 118356.

Sun, Y., Tong, C., Trainor-Guitton, W., et al. Global sampling for integrating physics-specific subsystems and quantifying uncertainties of CO_2 geological sequestration. Int. J. Greenhouse Gas Control 2013, 12: 108-123.

Taggart, I.J. Extraction of dissolved methane in brines by CO_2 injection: Implication for CO_2 sequestration. SPE Reserv. Eval. Eng. 2010, 13(5): 791-804.

Trevisan, L., Krishnamurthy, P., Meckel, T. Impact of 3d capillary heterogeneity and bedform architecture at the sub-meter scale on CO_2 saturation for buoyant flow in clastic aquifers. Int. J. Greenhouse Gas Control 2017, 56: 237-249.

Wallace, C.D., Sawyer, A.H., Soltanian, M.R., et al. Nitrate removal within heterogeneous riparian aquifers under tidal influence. Geophys. Res. Lett. 2020, 47(10): e2019GL085699.

Wang, J., Ryan, D., Anthony, E.J., et al. The effect of impurities in oxyfuel flue gas on CO_2 storage capacity. Int. J. Greenhouse Gas Control 2012, 11: 158-162.

Yang, F., Bai, B., Dunn-Norman, S. Modeling the effects of completion techniques and formation heterogeneity on CO_2 sequestration in shallow and deep saline aquifers. Environ. Earth Sci. 2011, 64(3): 841-849.

Yang, Z., Chen, Y.F., Niemi, A. Gas migration and residual trapping in bimodal heterogeneous media during geo-logical storage of CO_2. Adv. Water Resour. 2020, 142: 103608.

Zhang, L., Dilmore, R.M., Bromhal, G.S. Effect of outer boundary condition, reservoir size, and CO_2 effective permeability on pressure and CO_2 saturation predictions under carbon sequestration conditions. Greenhouse Gases 2016, 6(4): 546-560.

Zhang, L., Wang, Y., Miao, X., et al. Geochemistry in geologic CO_2 utilization and storage: A brief review. Adv. Geo-Energy Res. 2019, 3(3): 304-313.

Zhou, Y., Ritzi Jr, R.W., Soltanian, M.R., et al. The influence of streambed heterogeneity on hyporheic flow in gravelly rivers. Groundwater 2014, 52(2): 206-216.